Annals of Pure and Applied Mathematics
Vol. 31, No. 1, 2025, 31-52
ISSN: 2279-087X (P), 2279-0888(online)
Published on 18 February 2025
www.researchmathsci.org
DOI: http://dx.doi.org/10.22457/apam.v31n1a04957

Unsteady MHD Casson Fluid Flow through a Cylindrical Surface with Effects of Thermal Radiation and Chemical Reactivity

***Md. Rafiqul Islam*[1], *Md. Aslam Hossain*[1] and *Shaikh Khurram Alam*[2,*]**

[1]Department of Mathematics, Pabna University of Science and Technology
Pabna-6600, Bangladesh
[2]Mathematics Discipline, Khulna University, Khulna-9208, Bangladesh
[2]Email: khurram.alam05@gmail.com
[*]Corresponding author

Received 2 January 2025; accepted 2 February 2025

Abstract. This work's primary goal is to numerically model the phenomena of heat and mass transport in a non-Newtonian (Casson) fluid moving through a hydromagnetic cylindrical surface. However, this study's theoretical research looks into how heat radiation and higher-order chemical reactions affect MHD Casson fluid flow via a cylindrical surface. The flow-related equations must then be transformed into a non-dimensional form using a set of non-dimensional variables. The explicit finite difference technique (EFDM) is employed to simulate the fluid flow system numerically. Additionally, Compaq Visual FORTRAN 6.6. a computer code is generated. A stability and convergence study is conducted to evaluate the numerical method's correctness for the previously outlined research. It was found that when $\tau = 0.0005$, $\Delta X = 0.80$ and $\Delta R = 0.395$, the system converged at the Lewis number, $L_e \geq 0.020$, and the Prandtl number, $P_r \geq 0.055$. Additionally, a tabular and pictorial representation of the link between the system parameters and the skin friction coefficient, Nusselt number, and Sherwood number is provided. The use of streamlines and isothermal lines further illustrates the intricate visual depiction of fluid flow. After a final comparison, it is discovered that the current results and those that have already been published agree quite well.

Keywords: MHD, Casson Nanofluid, Thermal Radiation, EFD Method, Chemical Reaction

AMS Mathematics Subject Classification (2010): 76W05, 76E25

1. Introduction

Recent years have seen a significant increase in the use of non-Newtonian MHD fluids with nanoparticles (1-100nm) as opposed to Newtonian fluids. These fluids include Casson, Williamson, Carreau, micropolar, and tangent hyperbolic fluids, among others, and have numerous advantageous applications in both engineering and technology. There are three types of non-Newtonian fluids: viscoelastic, time-dependent, and time-independent. Other types are categorized as polar fluids, anisotropic fluids, visco-inelastic, viscoelastic, and microstructured fluids. Shear-thinning liquids, such as jelly, human blood,

tomato sauce, honey, cancer treatment, fibrinogen, blood cells, etc., are known as Casson fluids. They behave as a solid when shear stress is less than yield stress and as a fluid when shear stress is more than yield stress. Okay [1] used the Casson model to study a non-Newtonian blood model with capillaries in a weak wall. The lattice Boltzmann technique is used by Boyd et al. [2] to extract the Casson model's faithful and vibrating blood flow. The boundary-layer Casson model has recently attracted the attention of several authors due to its wide variety of applications. The presence of chemically reacting Casson fluid on porous surfaces has been investigated by Emmanuel et al. [3]. Malik et al. [4] have studied Casson nanofluid across an exponentially increasing vertical cylinder. Using the Laplace transformation, Hussanan et al. [5] describe the effects of heat transfer on unsteady Casson fluid boundary layer flow. The Casson nanofluid, which passes through a stretched sheet and incorporates a chemical reaction and a heat source/sink, was covered by Hayat et al. [6]. Soret, heat generation, thermal diffusion radiation, chemical reaction, and MHD Casson fluid flow via an oscillating vertical porous plate have all been examined by Makanda et al. [7], Mahabaleshwar & Lorenzini [8], Kataria and Patal [9], and others. In addition, Kataria and Patel [10] have investigated chemical reactions, heat generation, soret, and thermal diffusion radiation. Nadeem et al. [11] have considered the possibility of a magnetic field and Casson fluid past a diminishing sheet that is propelled exponentially. An inclined channel results from the peristaltic pumping Casson model, as reported by Kumari et al. [12]. On the other hand, Sreenadh et al. [13] created an inclined tube containing several neoplasms. Recent years saw the investigation of the Casson, Casson-Carreau, and Williamson nanofluids on an inclined cylindrical surface with various parameter effects by Sarkar et al. [14], [15], and [16].

Recently, fluid dynamics research has focused much on the investigation of chemical processes within the context of MHD and Casson fluids. Chemical reactions occurring in MHD Casson fluids can be explained by the reaction-diffusion term. Usually, these extra words explain how changes in the ratios of reactants and products over time are caused by chemical reactions and molecular diffusion. Numerous important subjects, including materials science, chemical engineering, and ecological science, can benefit greatly from the understanding of chemical reactions in MHD Casson fluids. Nandhini et al. [17] have created in parallel chemically reacted Casson fluid flow and radiation absorption via a steadily expanding surface under the influence of many exponential order flow features. The radiative characteristics of EMHD flow across the boundary layer with integrated thermal transport quality were examined by Asogwa et al. [18]. The thermal and mass transport properties of a non-Newton Casson–Williamson nanofluid flow were investigated by Yousef et al. [19]. When performing a numerical analysis of the heating effect on an unsteady MHD radiated and chemically reacted Casson hybrid nanofluid through a seemingly infinite oscillating vertical plate integrated into a porous system, Krishna [20] states that heat sink and viscous dissipation effects are taken into account. Researchers Biswas et al. [21] investigated the MHD Prandtl nanofluid exposed to thermal double diffusive flow over a considerably vertical surface in order to gain a better understanding of heat generation and the consequences of thermophoresis. Sayeed et al. [22] quantitatively investigated the physical properties of the unstable MHD nanofluid produced by the gyrotactic microbial cells using a cylindrical framework to simulate a two-dimensional scenario. Using a sheet of stretching in an apparition of Brownian motion, Biswas et al. [23] numerically analyzed the MHD flow behavior for a two-dimensional

Maxwell nanofluid. The effect of a stretched surface or vertical plate on the chemical bonding of different fluids has been studied by numerous research groups [24–33].

The impact of a chemical reaction on the free convection flow of a Casson nanofluid under a strong sinusoidal magnetic field has been studied very recently by Islam et al. [34]. Ahmed et al. [35] have explored the effects of thermal energy on magnetohydrodynamics in terms of chemical processes, thermal radiation, and the Brownian. Gautam et al. [36] proposed a comparison of the nonlinear thermal radiation impact of bio-convective MHD Casson and Maxwell nanofluids. The results indicated that the velocity of the Casson fluid was far more dominant than that of the Maxwell fluid. Both thermoelectric and radiation boost an MHD flow's heat transfer capacity, as demonstrated by Ali et al. [37] in a previous study. The main finding of the study is that the flow of nanofluid reduces with increasing heat radiation. The activation energy of Casson fluid and the primary role of nonlinear thermal radiation were previously studied by Reza-E-Rabbit et al. [38]. Additionally, it is found that heat transport is somewhat regulated by magnetism. Motivating the current work is a crucial observation made by the author that, under the impact of activation energy, nonlinear radiation considerably altered mass transmission down the wall, showing a substantial action of the fluid compared to a Newtonian one. In view of this, a recent study conducted by Li et al. [39] examined the impact of chemical reaction and activation energy on the magnetohydrodynamic (MHD) fluid flow resulting from Darcy-Forchheimer's Casson compression over porous media in a horizontal channel. Furthermore, Reddy et al. [40] examined mass and heat transfer in a hybrid nanoliquid flow across a stretching or contracting surface while taking into consideration various elements such as thermal radiation, chemical reactions, suction, and slip effects.

To the best of the author's knowledge, no research has been done on the magnetohydrodynamic flow of Casson nanofluid through a moving cylinder in the presence of heat radiation effects and chemical reactions. Therefore, it was deemed desirable to explore this subject in light of this knowledge gap, and the particular objectives of this paper were to:

a) Analyzing the Casson fluid model with the effects of radiation and chemical reaction reveals a cylindrical surface when a mathematical model is created.
b) To develop a numerical solution for the governing model pertaining to momentum, energy, and concentration equations using an explicit finite difference approach using the computer programming language Compact Visual FORTRAN 6.6.a.
c) To evaluate the fluid flow system's stability and convergence tests.
d) To analyze the temperature, velocity, and concentration distribution of the Casson fluids as well as streamlines, isotherms, skin friction, Sherwood number, and Nusselt number with different physical properties.

2. Mathematical analysis

This study has focused on the unsteady magnetohydrodynamic (MHD) current of a Casson nanofluid flowing in a vertical cylinder. Thermal radiation is present in the founding fluids of this model, which includes higher-order chemical reactions. The x axis is selected in the upward direction of the cylinder, while the radial coordinate r is selected normal to the

surface, where the cylinder's radius is r_0. On the cylindrical surface that is occupied by electrically non-conducting material, the same external magnetic region B_0 is applied. The posterior **Figure 1** shows the physical model and coordinate strait of this investigation.

The cylinder's main velocity is u_0, and its elementary temperature and pressure are $\bar{T}_\infty$ and $\bar{C}_\infty$. The higher temperature and concentration on the cylindrical surface are related to $\bar{T}_w$ and $\bar{C}_w$, respectively, where $\bar{T}_w > \bar{T}_\infty$ and $\bar{C}_w > \bar{C}_\infty$.
Based on these presumptions, the flow model is provided by;

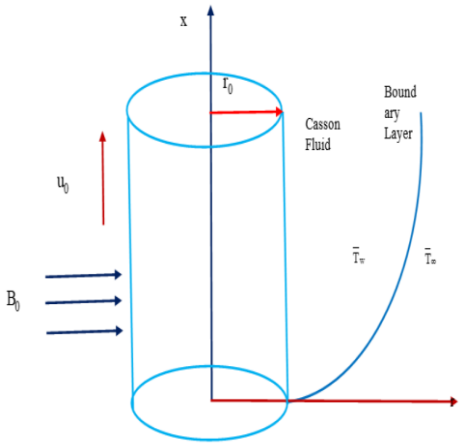

Figure 1. Geometric configuration of flow model

Continuity equation:

$$\frac{\partial(ru)}{\partial x}+\frac{\partial(rv)}{\partial r}=0 \tag{1}$$

Momentum Equation:

$$\frac{\partial u}{\partial t}+u\frac{\partial u}{\partial x}+v\frac{\partial u}{\partial r}=\nu\left(1+\frac{1}{\beta}\right)\left(\frac{\partial^2 u}{\partial r^2}+\frac{1}{r}\frac{\partial u}{\partial r}\right)+g\beta_{\bar{T}}(\bar{T}-\bar{T}_\infty)$$
$$+g\beta_{\bar{C}}(\bar{C}-\bar{C}_\infty)-\frac{\sigma B_0^2 \mathrm{u}}{\rho} \tag{2}$$

Energy Equation:

$$\frac{\partial \bar{T}}{\partial t}+u\frac{\partial \bar{T}}{\partial x}+v\frac{\partial \bar{T}}{\partial r}=\frac{k}{\rho c_p}\left(\frac{\partial^2 \bar{T}}{\partial r^2}+\frac{1}{r}\frac{\partial \bar{T}}{\partial r}\right)+\tau\left[D_{\bar{B}}\left(\frac{\partial \bar{C}}{\partial r}.\frac{\partial \bar{T}}{\partial r}\right)+\frac{D_T}{\bar{T}_\infty}\left(\frac{\partial \bar{T}}{\partial r}\right)^2\right]$$
$$-\frac{1}{\rho c_p}\frac{1}{r}\frac{\partial}{\partial r}(rq_r)+\frac{Q_0}{\rho c_p}(\bar{T}-\bar{T}_\infty) \tag{3}$$

Concentration Equation:

$$\frac{\partial \bar{C}}{\partial t}+u\frac{\partial \bar{C}}{\partial x}+v\frac{\partial \bar{C}}{\partial r}=D_{\bar{B}}\left(\frac{\partial^2 \bar{C}}{\partial r^2}+\frac{1}{r}\frac{\partial \bar{C}}{\partial r}\right)+\frac{D_T}{\bar{T}_\infty}\left(\frac{\partial^2 \bar{T}}{\partial r^2}+\frac{1}{r}\frac{\partial \bar{T}}{\partial r}\right)-K_c(\bar{C}-\bar{C}_\infty)^{\mathrm{p}} \tag{4}$$

Boundary conditions are

$$\left.\begin{array}{llll} t\le 0: u=0, v=0, \bar{T}=\bar{T}_\infty, \bar{C}=\bar{C}_\infty \text{ for every where} & & & \\ t>0:\ u=u_0, & v=0, & \bar{T}=\bar{T}_w, & \bar{C}=\bar{C}_w \quad at\ r=r_0 \\ u=0, v=0, \bar{T}=\bar{T}_\infty, & \bar{C}=\bar{C}_\infty & at\ x=0; r\ge r_0 & \\ u\to 0, v\to 0, & \bar{T}\to\bar{T}_\infty, & \bar{C}\to\bar{C}_\infty & as\ r\to\infty \end{array}\right\} \tag{5}$$

For radiative heat flux, the Rosseland approximation becomes $q_r=-\frac{4\acute{\sigma}}{3k_s}\frac{\partial \bar{T}^4}{\partial y}$. Assuming a relatively small temperature differential in the flow, we adopt the expression $\bar{T}^4 \approx 4\bar{T}_\infty^3\bar{T}-3\bar{T}_\infty^4$ and express $\bar{T}^4$ by Tailor's estimate at $\bar{T}_\infty$. (Terms with higher rankings are dropped). As a result, the solution to equation (3) is

$$\frac{\partial \bar{T}}{\partial t}+u\frac{\partial \bar{T}}{\partial x}+v\frac{\partial \bar{T}}{\partial r}=\frac{k}{\rho c_p}\left(\frac{\partial^2 \bar{T}}{\partial r^2}+\frac{1}{r}\frac{\partial \bar{T}}{\partial r}\right)+\tau\left[D_{\bar{B}}\left(\frac{\partial \bar{C}}{\partial r}.\frac{\partial \bar{T}}{\partial r}\right)+\frac{D_T}{\bar{T}_\infty}\left(\frac{\partial \bar{T}}{\partial r}\right)^2\right]$$
$$+\frac{16\acute{\sigma}\bar{T}_\infty^3}{3k_s\rho c_p}\frac{1}{r}\frac{\partial}{\partial r}\left(r\frac{\partial \bar{T}}{\partial r}\right)+\frac{Q_0}{\rho c_p}(\bar{T}-\bar{T}_\infty) \quad (6)$$

The following dimensionless portions are used for dimensionless:

$$X=\frac{x\nu}{u_0 r_0^2}, R=\frac{r}{r_0}, U=\frac{u}{u_o}, V=\frac{vr_0}{\nu}, \tau=\frac{t\nu}{r_0^2}, T=\frac{\bar{T}-\bar{T}_\infty}{\bar{T}_w-\bar{T}_\infty}, C=\frac{\bar{C}-\bar{C}_\infty}{\bar{C}_w-\bar{C}_\infty}$$

The dimensionless variables are used to build the coupled nonlinear partial differential equations that are shown below:

Continuity equation:

$$\frac{\partial(RU)}{\partial X}+\frac{\partial(RV)}{\partial R}=0 \quad (7)$$

Momentum Equation:

$$\frac{\partial U}{\partial \tau}+U\frac{\partial U}{\partial X}+V\frac{\partial U}{\partial R}=\left(1+\frac{1}{\beta}\right)\left(\frac{\partial^2 U}{\partial R^2}+\frac{1}{R}\frac{\partial U}{\partial R}\right)\left[+\left(\frac{\partial T}{\partial Y}\frac{\partial U}{\partial Y}\right)\right]$$
$$+G_rT+G_mC-MU \quad (8)$$

Energy Equation:

$$\frac{\partial T}{\partial \tau}+U\frac{\partial T}{\partial X}+V\frac{\partial T}{\partial R}=\frac{1}{P_r}\left(1+\frac{4}{3R_a}\right)\left(\frac{\partial^2 T}{\partial R^2}+\frac{1}{R}\frac{\partial T}{\partial R}\right)$$
$$+N_b\left(\frac{\partial C}{\partial R}\frac{\partial T}{\partial R}\right)+N_t\left(\frac{\partial T}{\partial R}\right)^2+QT \quad (9)$$

Concentration Equation:

$$\frac{\partial C}{\partial \tau}+U\frac{\partial C}{\partial X}+V\frac{\partial C}{\partial R}=\frac{1}{L_e}\left[\left(\frac{\partial^2 C}{\partial R^2}+\frac{1}{R}\frac{\partial C}{\partial R}\right)+\left(\frac{N_t}{N_b}\right)\left(\frac{\partial^2 T}{\partial R^2}+\frac{1}{R}\frac{\partial T}{\partial R}\right)\right]-K_r(C)^p \quad (10)$$

Corresponding boundary conditions are

$$\left.\begin{array}{l}\tau\le 0: U=0, V=0, T=0, C=0 \ \text{ for every where}\\ \tau>0:\ U=1,\ V=0,\quad T=1,\quad C=1\ \ at\ R=1\\ U=0, V=0, T=0,\ C=0\quad at\ X=0; R\ge 1\\ U\to 0, V\to 0,\ T\to 0,\quad C\to 0\quad as\ R\to\infty\end{array}\right\} \quad (11)$$

where $G_r=\frac{g\beta_{\bar{T}}r_0^2(\bar{T}_w-\bar{T}_\infty)}{\nu u_0}$, $G_m=\frac{g\beta_{\bar{T}}r_0^2(\bar{C}_w-\bar{C}_\infty)}{\nu u_0}$, $M=\frac{\sigma B_0^2 r_0^2}{\rho\nu}$, $P_r=\frac{\nu\rho c_p}{\kappa}$,
$N_t=\frac{\tau D_T(\bar{T}_w-\bar{T}_\infty)}{\nu\bar{T}_\infty}$, $N_b=\frac{\tau D_{\bar{B}}(\bar{C}_w-\bar{C}_\infty)}{\nu}$, $L_e=\frac{\nu}{D_B}$, $R_a=\frac{kk_s}{4\acute{\sigma}\bar{T}_\infty^3}$, $Q=\frac{Q_0 r_0^2}{\rho c_p\nu}$,
$K_r=\frac{K_c r_0^2(\bar{C}_w-\bar{C}_\infty)^{p-1}}{\nu}$.

The following form is used to calculate the skin frictions $C_f=-\frac{1}{2\sqrt{2}}\left(\frac{\partial U}{\partial R}\right)_{R=0}$, Nusselt number, $N_u=\frac{1}{\sqrt{2}}\left(\frac{\partial T}{\partial R}\right)_{R=0}$ and Sherwood number $S_h=\frac{1}{\sqrt{2}}\left(\frac{\partial C}{\partial R}\right)_{R=0}$, which are physical non-dimensional quantities.

The continuity equations that are directly related to the velocity components are satisfied by the stream function ψ, which may be written as $U = \frac{\partial \psi}{\partial Y}, V = -\frac{\partial \psi}{\partial X}$.

3. Numerical solutions

In this section, the principal dimensionless partial differential equations associated with the nonlinearity of the second order and their corresponding boundary conditions are solved. In light of the preceding discussion, equations (7) through (10) have been easily solved using the EFD approach while adhering to the conditions of (11). In order to derive the finite difference equations, the Casson nanofluid flow province is divided into longitudinal grids or meshes oriented in the directions X and R, which correspond to the apprehend axis and the cylinder's normal (**Figure-2**).In this case, we consider R_{max} $(= 50)$ to correspond to $R \to \infty$ and assume that the cylinder has a maximum height of X_{max} $(= 100)$, where X spans from 0 to 100. The subscripts i and j denote the grid points toward the X and R coordinates respectively, where $X = i\Delta X$ and $R = 1 + (j-1)\Delta R, m = 125$ and $n = 125$ grid spacing in the X and R directions respectively. The altitude is $\Delta X = 0.80$, $\Delta R = 0.395$ and the small time difference $\Delta\tau = 0.0005$.

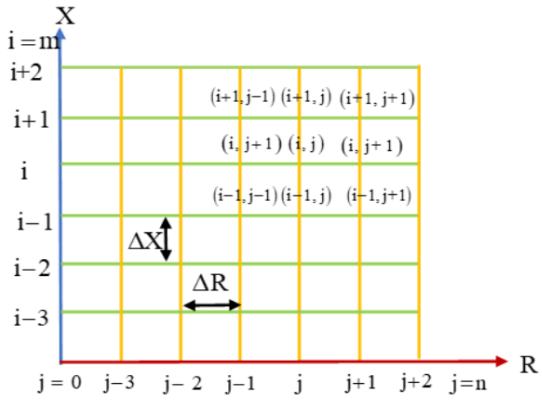

Figure 2. Finite difference space

Equations (7) through (11) are now converted into the finite difference form shown below:

$$\frac{U_{i,j} - U_{i-1,j}}{\Delta X} + \frac{V_{i,j} - V_{i-1,j}}{\Delta R} + \frac{V_{i,j}}{1 + (j-1)\Delta R} = 0 \tag{12}$$

$$\frac{\acute{U}_{i,j} - U_{i,j}}{\Delta\tau} + U_{i,j}\left(\frac{U_{i,j} - U_{i-1,j}}{\Delta X}\right) + V_{i,j}\left(\frac{U_{i,j+1} - U_{i,j}}{\Delta R}\right) =$$
$$\left(1 + \frac{1}{\beta}\right)\left[\left(\frac{U_{i,j+1} - 2U_{i,j} + U_{i,j-1}}{(\Delta R)^2}\right) + \frac{1}{1 + (j-1)\Delta R}\left(\frac{U_{i,j+1} - U_{i,j}}{\Delta R}\right)\right]$$
$$-MU_{i,j} + G_r T_{i,j} + G_m C_{i,j} \tag{13}$$

$$\frac{\acute{T}_{i,j} - T_{i,j}}{\Delta\tau} + U_{i,j}\left(\frac{T_{i,j} - T_{i-1,j}}{\Delta X}\right) + V_{i,j}\left(\frac{T_{i,j+1} - T_{i,j}}{\Delta R}\right) =$$
$$\frac{1}{P_r}\left(1 + \frac{4}{3R_a}\right)\left[\left(\frac{T_{i,j+1} - 2T_{i,j} + T_{i,j-1}}{(\Delta R)^2}\right) + \frac{1}{1 + (j-1)\Delta R}\left(\frac{T_{i,j+1} - T_{i,j}}{\Delta R}\right)\right]$$
$$+N_b\left(\frac{C_{i,j+1} - C_{i,j}}{\Delta R}\right)\left(\frac{T_{i,j+1} - T_{i,j}}{\Delta R}\right) + N_t\left(\frac{T_{i,j+1} - T_{i,j}}{\Delta R}\right)^2 + QT_{i,j} \tag{14}$$

$$\frac{\acute{C}_{i,j} - C_{i,j}}{\Delta\tau} + U_{i,j}\left(\frac{C_{i,j} - C_{i-1,j}}{\Delta X}\right) + V_{i,j}\left(\frac{C_{i,j+1} - C_{i,j}}{\Delta R}\right) =$$
$$\frac{1}{L_e}\left[\left(\frac{C_{i,j+1} - 2C_{i,j} + C_{i,j-1}}{(\Delta R)^2}\right) + \frac{1}{1 + (j-1)\Delta R}\left(\frac{C_{i,j+1} - C_{i,j}}{\Delta R}\right)\right]$$

$$+\left(\frac{N_t}{N_b.L_e}\right)\left[\left(\frac{T_{i,j+1}-2T_{i,j}+T_{i,j-1}}{(\Delta R)^2}\right)+\frac{1}{1+(j-1)\Delta R}\left(\frac{T_{i,j+1}-T_{i,j}}{\Delta R}\right)\right]$$
$$-K_r\left(C_{i,j}\right)^p \qquad (15)$$

Converting boundary conditions are:

$$\left.\begin{array}{lll} \tau \le 0; \quad U_j^0 = 0 & T_j^0 = 0 & C_j^0 = 0 \quad \text{every where} \\ \tau > 0; \; U_j^0 = 1 & T_j^0 = 1 & C_j^0 = 1 \text{ for all } R = 1 \\ U_j^n = 0 & T_j^n = 0 & C_j^n = 0 \quad as \quad R \to \infty \end{array}\right\} \qquad (16)$$

4. Convergence and stability study

The stability conditions for this experiment are established as (Islam M.R. et al [34]):

$$\frac{1}{P_r}\left\{\left(1+\frac{4}{3R_a}\right)\frac{2\Delta\tau}{(\Delta R)^2}+\frac{\Delta\tau}{R\Delta R}\right\}-N_bC\frac{2\Delta\tau}{(\Delta R)^2}-N_tT\frac{2\Delta\tau}{(\Delta R)^2}-Q.\frac{\Delta\tau}{2}+U\frac{\Delta\tau}{\Delta X}+|-V|\frac{\Delta\tau}{\Delta R} \le 1$$

$$\left(\frac{1}{L_e}\right)\left\{\frac{2\Delta\tau}{(\Delta R)^2}+\frac{\Delta\tau}{R\Delta R}\right\}+K_r(C)^{p-1}.\frac{\Delta\tau}{2}+U\frac{\Delta\tau}{\Delta X}+|-V|\frac{\Delta\tau}{\Delta R} \le 1$$

At $\tau = 0$, the primary boundary conditions are $U = V = T = C = 0$. The convergence criterion for the current problem would be set for $P_r \ge 0.055$ and $L_e \ge 0.020$, when $\Delta\tau = 0.0005, \Delta X = 0.80$, and $\Delta R = 0.39$.

5. Verification of the results

A tabular validation/comparison of the results with published work Sarker et al. [14]:

Table 1:

Increased Parameter	Present Result			Sarker et al. [14]		
	U	T	C	U	T	C
Magnetic parameter (M)	Dec.	-	-	Dec.	Inc.	-
Prandtl number (P_r)	Dec.	Dec.	Inc.	-	Dec.	-
Grashof number (G_r)	Inc.	-	-	Inc.	-	-
Heat source parameter (Q)	Inc.	Inc.	Dec.	-	-	Dec.
Radiation parameter (R_a)	-	Dec.	Inc.	-	-	-
Lewis number (L_e)	-	-	Dec.	-	-	Dec.
Chemical reaction (K_r)	-	-	Dec.	Inc.	-	-
Casson term (β)	Dec.	-	-	Dec.	-	-

N.B.: Inc. for increase and Dec. for decrease.

6. Results and discussions

The numerical investigation of the two-dimensional boundary layer flow of an unstable, MHD Casson fluid through a cylindrical surface has been conducted. To illustrate the

physical sagacity of this study, a number of parameters have been plotted, including the Casson fluid parameter (β), Prandtl number (P_r), magnetic parameter (M), Brownian motion (N_b), thermophoresis (N_t), Lewis number (L_e), Mass Grashof number (G_r), thermal grashof number (G_m), Chemical reaction parameter (K_r), thermal radiation parameter (R_a), and others. These profiles include velocity, temperature, concentration, skin friction, Nusselt number, Sherwood number, streamlines, and isothermal lines. The primary parameters' values that are regarded as $M = 1.0, N_b = 0.1, G_r = 10.0, R_a = 1.0, P_r = 1.0, N_t = 0.1,\ G_m = 1.0, L_e = 1.0, \beta = 0.1, K_r = 0.5, Q = 0.1$ **Figures-3** to **20** illustrate the effects of the aforementioned parameters on the velocity, temperature, concentration, skin friction, Nusselt number Sherwood number, streamlines and isothermal lines profiles. The Casson nano-fluid is examined and developed in this work using explicit finite difference simulation. The study of Sarker et al. [14] provided qualitative validation for the current numerical simulation (**see Table 1**).

Figure. 3 illustrates the magnetic parameter's structural structure for velocity fields. The Lorentz force is produced in a system when there is a magnetic field present. The fluid's rate of motion is decreased by this force. The fluid velocity decreases as a result of this force. As M grows from 1.00 to 9.00, the curve-to-curve fluctuation for velocity profiles decreases by 22.40%, 17.28%, 13.25%, and 9.78%, respectively at $R = 3.00$.

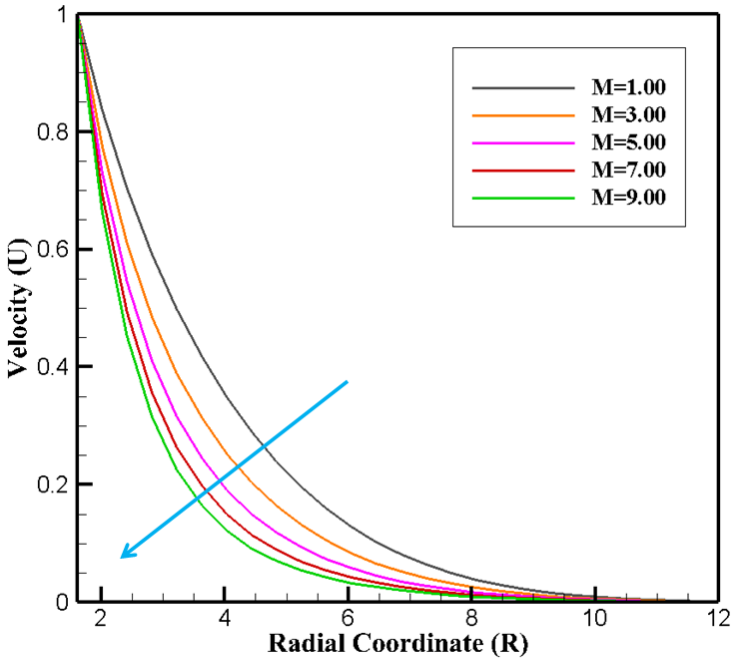

Figure 3: The impact of M on velocity fields, when $Q = 0.1, P_r = 1.0, G_m = 1.0, N_t = 0.1, N_b = 0.1, L_e = 1.0, \beta = 0.1, K_r = 0.5, G_r = 1.0, R_a = 0.1$.

The shift in the velocity characteristic resulting from the Grashof number (G_r) is seen in **Figure-4**, where the velocity increases as the parameter increases. A buoyancy parameter increase can promote more particle contact and raise the velocity field, which in turn increases the dominance of buoyant forces in the flow. At $R = 3.00$, the velocity profiles exhibit an increase in curve-to-curve variation of 23.50%, 21.45%, 20.25%,

and 18.68% when $G_r$increases from 1.00 to 3.00. The effect of the Casson term (β) is illustrated in **Figure-5.** This tendency and the velocity depreciation are caused by an increase in the viscous forces acting on the flow with the addition of Casson fluid. **Figure-6** illustrates the influence of heat generation (Q) on velocity profiles. It is observed that the velocity silhouettes are augmented in the term of increased heat generation due to the increase in boundary layer thickness.

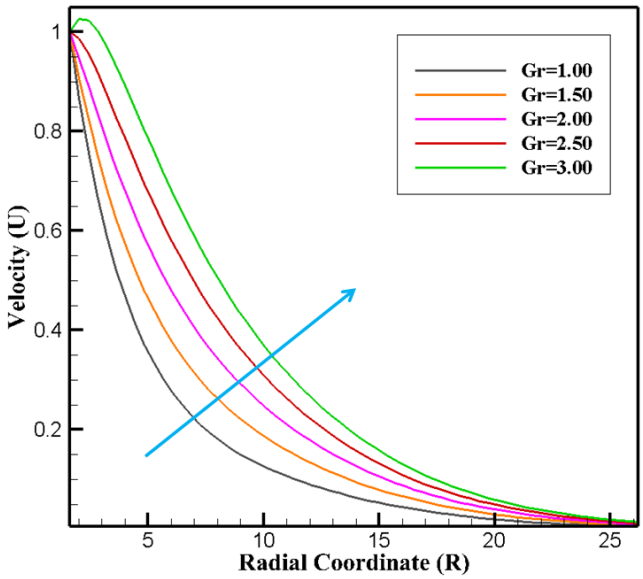

Figure 4: The impact of G_r on velocity fields, when $Q = 0.1, M = 1.0, G_m = 1.0, N_t = 0.1, N_b = 0.1, L_e = 1.0, \beta = 0.1, K_r = 0.5, P_r = 1.0, R_a = 0.1.$

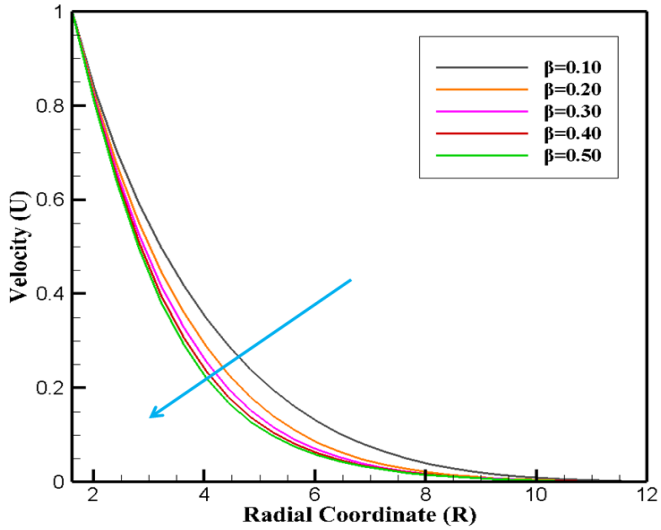

Figure 5: The impact of β on velocity fields, when $Q = 0.1, M = 1.0, G_m = 1.0, N_t = 0.1, N_b = 0.1, L_e = 1.0, P_r = 1.0, K_r = 0.5, G_r = 1.0, R_a = 0.1.$

Figure-7 displays the temperature silhouettes of the heat source parameter. An increased temperature is produced by the particles' increased involvement due to heat

generation's capacity to store energy. At $R = 3.00$, the temperature profiles exhibit an increase in curve-to-curve variation of 45.40%, 42.36%, 38.29%, and 35.78% when Q increases from 1.00 to 5.00. Numerous industrial processes involve the influence of thermal radiation.

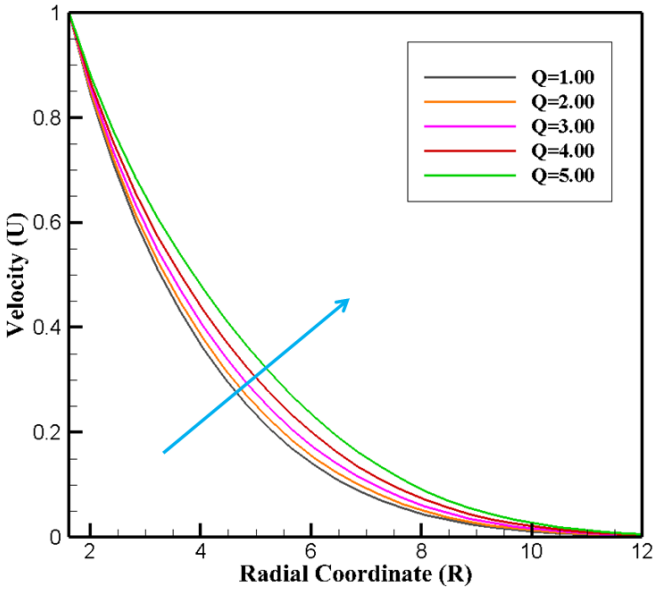

Figure 6: The impact of Q on velocity fields, when $\beta = 0.1, M = 1.0, G_m = 1.0, N_t = 0.1, N_b = 0.1, L_e = 1.0, P_r = 1.0, K_r = 0.5, G_r = 1.0, R_a = 0.1$.

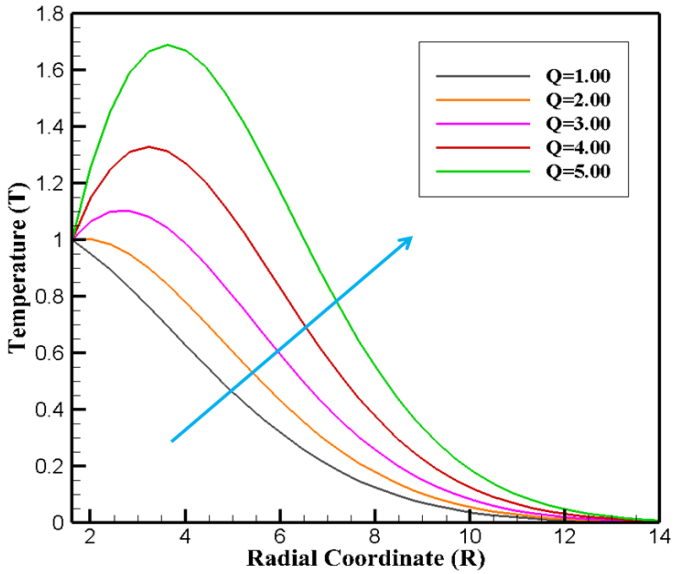

Figure 7: The influence of Q on temperature fields, when $\beta = 0.1, M = 1.0, G_m = 1.0, N_t = 0.1, N_b = 0.1, L_e = 1.0, P_r = 1.0, K_r = 0.5, G_r = 1.0, R_a = 0.1$.

It is necessary to comprehend how a number of significant factors affect temperature profiles. In **Figure 8**, the temperature distribution for the Prandtl number is also displayed. In fluids with lower Prandtl values, thermodynamic conductivities are higher

and improved. Therefore, by applying the Prandtl number, conductive fluids can be cooled more quickly.

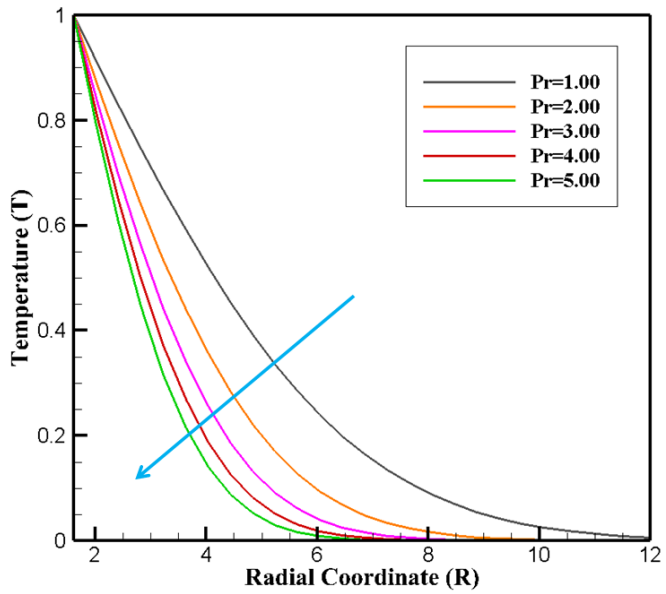

Figure 8: The influence of P_r on temperature fields, when $\beta = 0.1, M = 1.0, G_m = 1.0, N_t = 0.1, N_b = 0.1, L_e = 1.0, Q = 0.1, K_r = 0.5, G_r = 1.0, R_a = 0.1.$

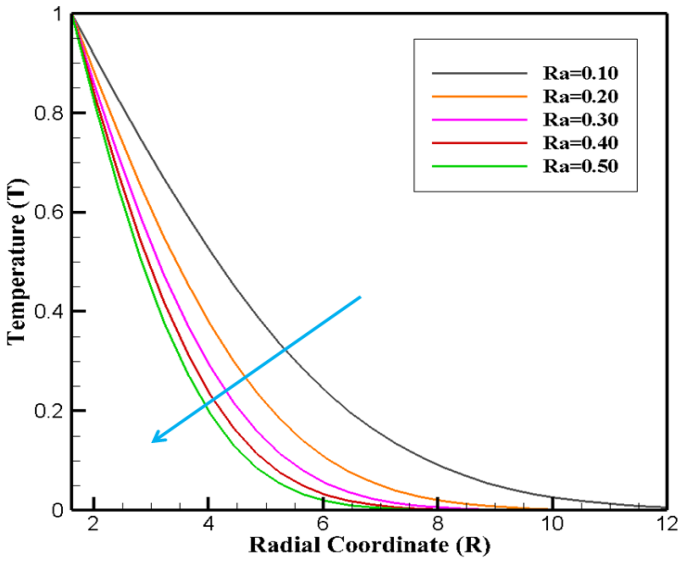

Figure 9: The influence of R_a on temperature fields, when $\beta = 0.1, M = 1.0, G_m = 1.0, N_t = 0.1, N_b = 0.1, L_e = 1.0, Q = 0.1, K_r = 0.5, G_r = 1.0, P_r = 1.0.$

The effect of the radiation parameter (R_a) on temperature profiles may be seen in **Figure-9**. It shows that as R_a increases, the thickness of the flow field falls by 55.52%,

35.32%, 20.67% and by 12.41%, respectively, from 0.10 to 0.20, 0.20 to 0.30, 0.30 to 0.40 and 0.40 to 0.50.

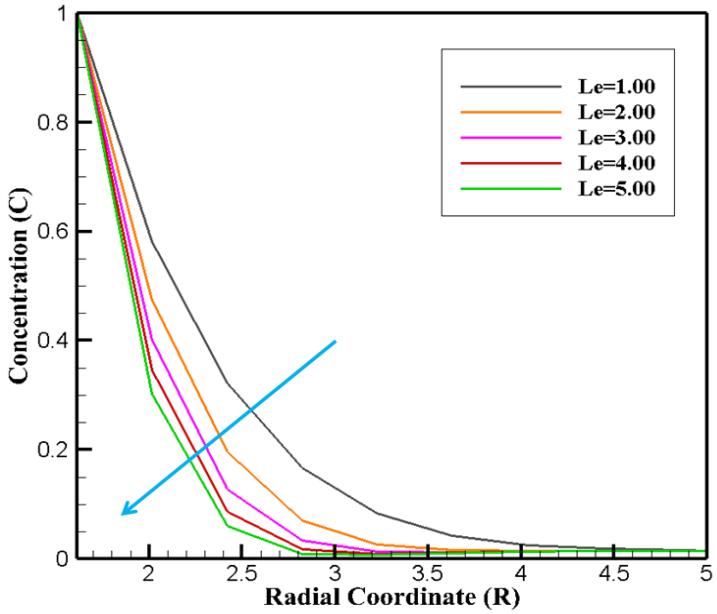

Figure 10: The impression of L_e on concentration fields, when $\beta = 0.1, M = 1.0, G_m = 1.0, N_t = 0.1, N_b = 0.1, K_r = 0.5, Q = 0.1, R_a = 0.1, G_r = 1.0, P_r = 1.0$.

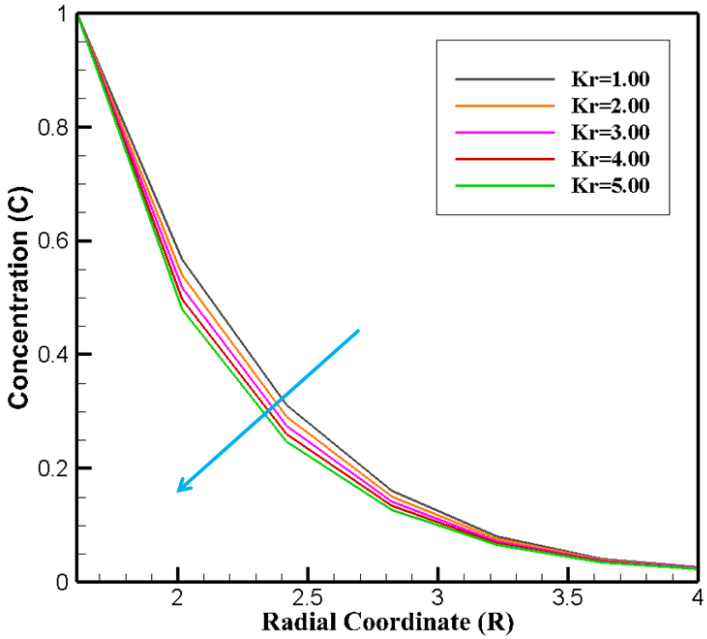

Figure 11: The impression of K_r on concentration fields, when $\beta = 0.1, M = 1.0, G_m = 1.0, N_t = 0.1, N_b = 0.1, L_e = 1.0, Q = 0.1, R_a = 0.1, G_r = 1.0, P_r = 1.0$.

The viscosity of the concentration and thermal boundary coatings is compared using the Lewis number. **Figure 10** makes a suggestion about how the Lewis number influences the concentration silhouette. As the concentration boundary layer thickness decreases, there is an increase in Lewis number.

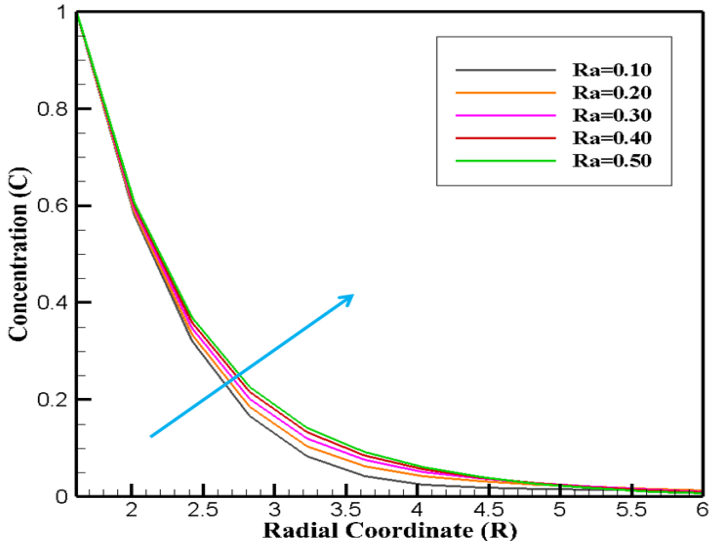

Figure 12: The impression of R_a on concentration fields, when $\beta = 0.1, M = 1.0, G_m = 1.0, N_t = 0.1, N_b = 0.1, L_e = 1.0, Q = 0.1, P_r = 1.0, G_r = 1.0, K_r = 0.5$.

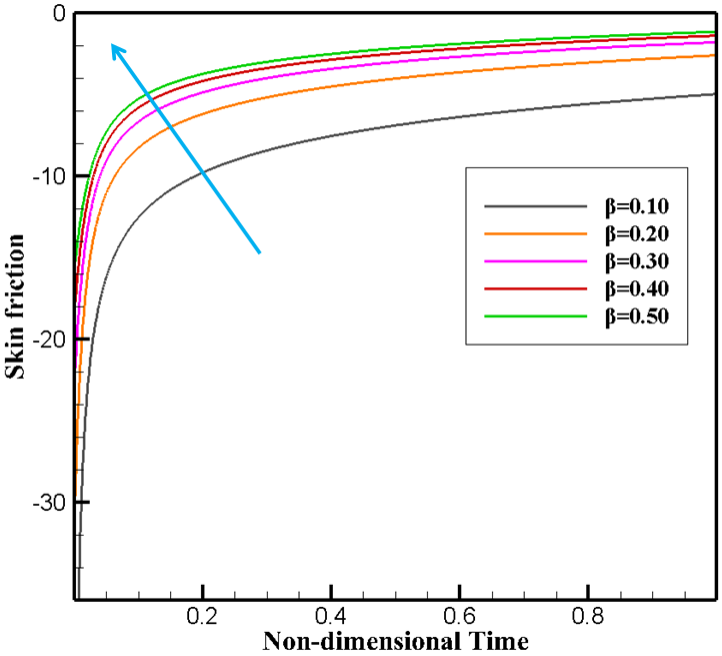

Figure 13: Variation of β on C_f, when $R_a = 0.1, M = 1.0, G_m = 1.0, N_t = 0.1, N_b = 0.1, L_e = 1.0, Q = 0.1, P_r = 1.0, G_r = 1.0, K_r = 0.5$.

Furthermore, as can be observed in **Figure 11**, the concentration fields get narrower when the higher-order chemical reaction (K_r) parameter rises. A more disruptive and damaging chemical reaction physically influences the concentric outlines that enable the maturation of molecular mobility and an increase in the spectacle of heat transmission.

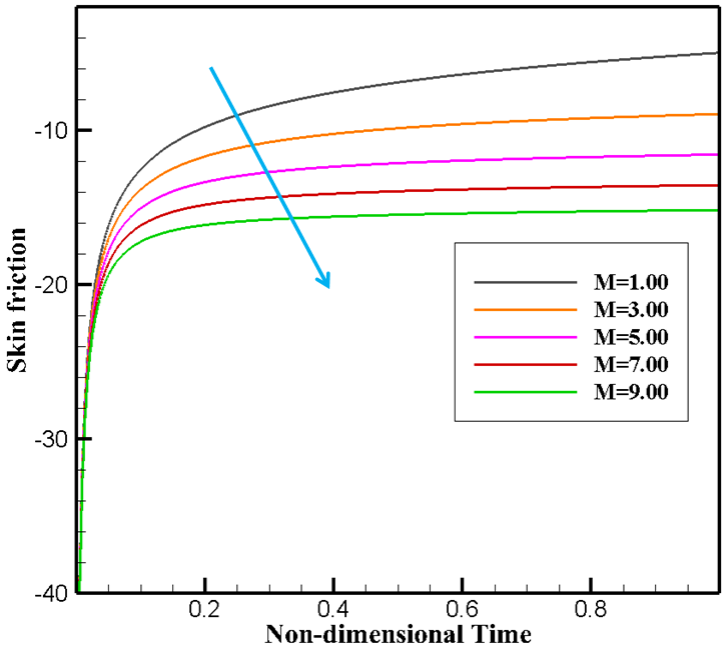

Figure 14: Variation of M on C_f, when $R_a = 0.1, G_r = 1.0, G_m = 1.0, N_t = 0.1, N_b = 0.1, L_e = 1.0, Q = 0.1, P_r = 1.0, \beta = 0.1, K_r = 0.5$.

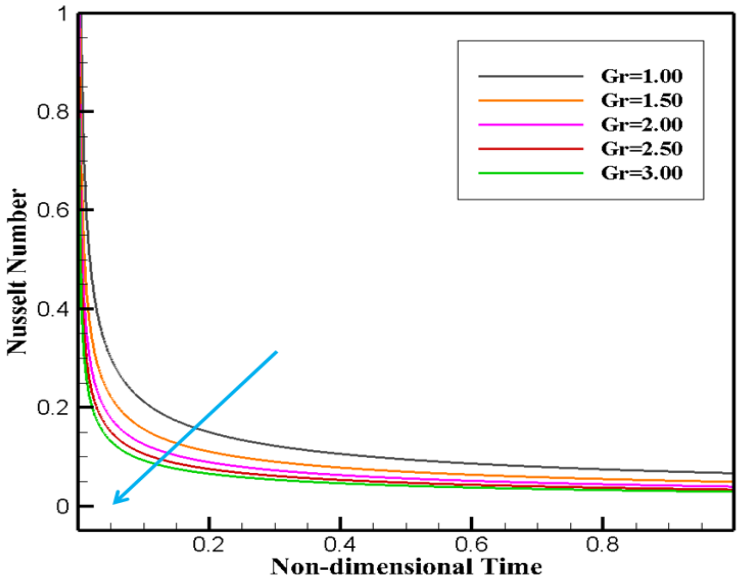

Figure 15: Variation of G_r on N_u, when $R_a = 0.1, M = 1.0, G_m = 1.0, N_t = 0.1, N_b = 0.1, L_e = 1.0, Q = 0.1, P_r = 1.0, \beta = 0.1, K_r = 0.5$.

The effect of the radiation parameter on the concentration field is shown in **Figure 12**. A rising profile is values that rise overproduced by thermal radiation time. In **Figures 13** and **14**, respectively, the skin friction silhouettes are remembered to be gradients as a result of the accumulation of the Casson term $(\beta)$and magnetic parameter (M). **Figure 13** shows how skin friction acts in the presence of Casson parameter effects. With an increase in Casson values, it has been observed that skin friction increases. It has been noted that skin friction profiles rise for increasing all parameter values of the Casson term.

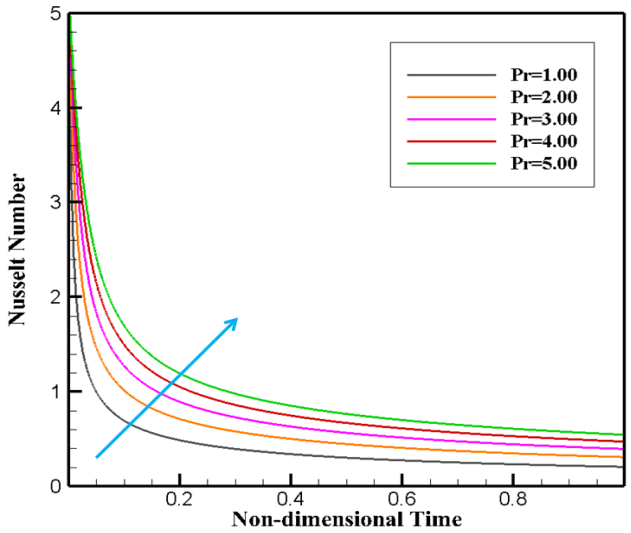

Figure 16: Variation of P_r on N_u, when $R_a = 0.1, M = 1.0, G_m = 1.0, N_t = 0.1, N_b = 0.1, L_e = 1.0, Q = 0.1, G_r = 1.0, \beta = 0.1, K_r = 0.5$.

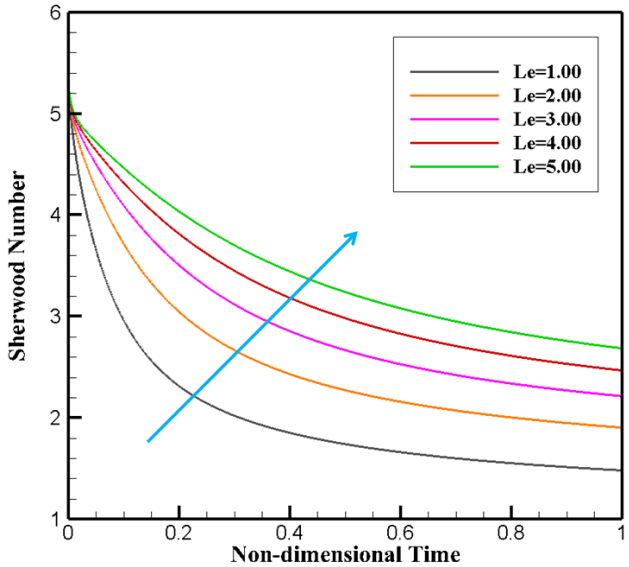

Figure 17: Variation of L_e on S_h, when $R_a = 0.1, M = 1.0, G_m = 1.0, N_t = 0.1, N_b = 0.1, G_r = 1.0, Q = 0.1, P_r = 1.0, \beta = 0.1, K_r = 0.5$.

The skin friction profiles for different values of the magnetic parameter (M) are shown in **Figure 14**. It is executed that with the increase of M skin friction profiles decrease and the decreasing rate is 30.52% from $M = 1.0\ to\ 3.0$, 28.33% from $M = 3.0\ to\ 5.0$ 27.24% from $M = 5.0\ to\ 7.0$ and 25.55% from $M = 7.0\ to\ 9.0$. **Figures 15** and **16** show the effects of various characteristics on the Nusselt number, including the Grashof number and the Prandlt number. In comparison to the curve for $G_r = 3.0$, **Figure 15** shows that the Nusselt number for $G_r = 1.0$ is considerably improved. With respect to the Grashof number, the N_u decreasing rate is 18.26% at $\tau = 1.0$ from $G_r = 1.0\ to\ 1.5$, 14.42% from $G_r = 1.5\ to\ 2.0$, 8.79% from $G_r = 2.0\ to\ 2.5$ and 4.60% from $G_r = 2.5\ to\ 3.0$. The Nusselt number for $P_r = 1.0$ is shown in **Figure-16**, which shows a more improved curve than that of $P_r = 5.0$. The growing rate of N_u, as measured by the Prandtl number,

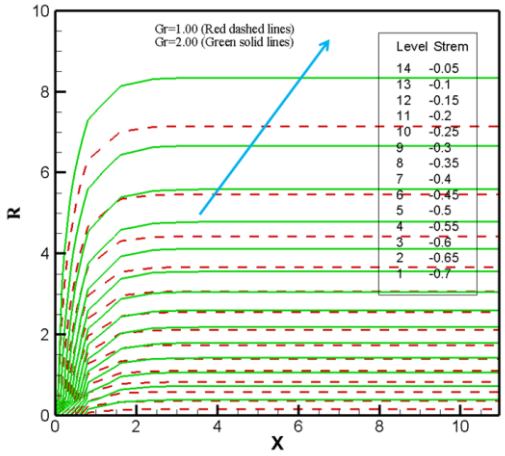

Figure 18 (a): Streamlines (contour view) for $G_r = 1.00, 2.00$.

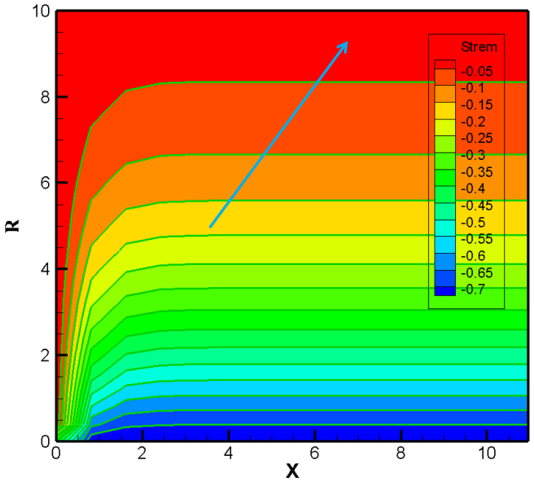

Figure 18 (b): Streamlines (flood and line view) for $G_r = 1.00, 2.00$.

at $\tau = 1.0$ are 25.67% from $P_r = 1.0\ to\ 2.0$, 20.98% from $P_r = 2.0\ to\ 3.0$, 16.46% from $P_r = 3.0\ to\ 4.0$ and 12.36% from $P_r = 4.0\ to\ 5.0$. The effects of the Lewis number on the Sherwood number is displayed in **Figure-17**. The Sherwood number increases at a rate of

52.55% from $L_e = 1.0\ to\ 2.0$, 45.56% from $L_e = 2.0\ to\ 3.0$, 34.32% from $L_e = 3.0\ to\ 4.0$ and 26.51% from $L_e = 4.0\ to\ 5.0$ at $\tau = 1.0$, according to the change in the Lewis number.

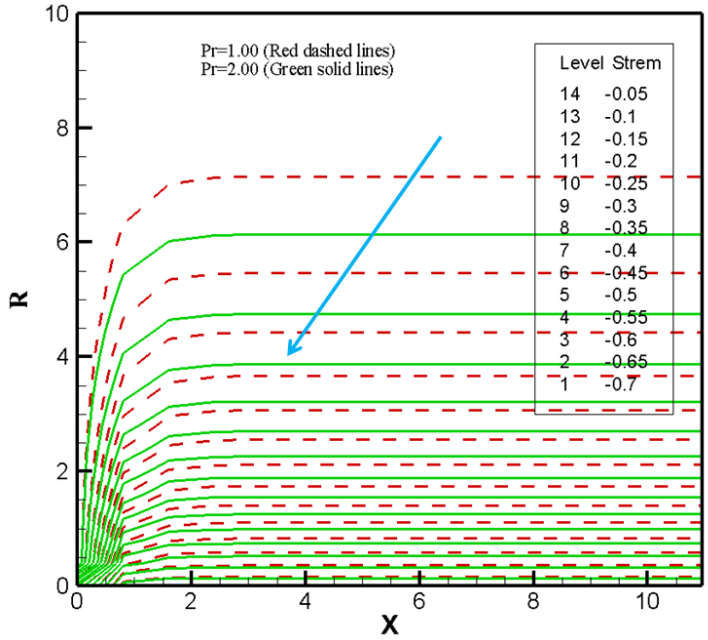

Figure 19 (a): Streamlines (contour view) for $P_r = 1.00, 2.00$.

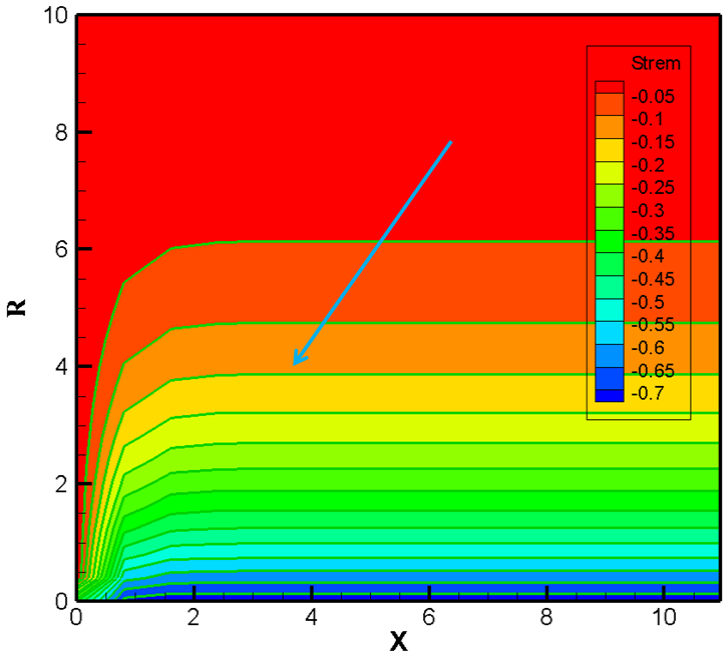

Figure 19 (b): Streamlines (flood and line view) for $P_r = 1.00, 2.00$.

Using streamlines and isothermal stripes in flood and line feelings, we can finally use the difference between the boundary layer for various parameters to explain the phenomenon. **Figures 18** to **20** show how streamlines and isotherms have an impact. **Figures 18 (a)** to **19(a)** show that streamlines (contour view) develop as a result of increasing Grashof number values from $G_r = 1.0\ to\ P_r = 2.0$, but diminish as a result of improved Prandtl number from $P_r = 1.0\ to\ G_r = 2.0$.

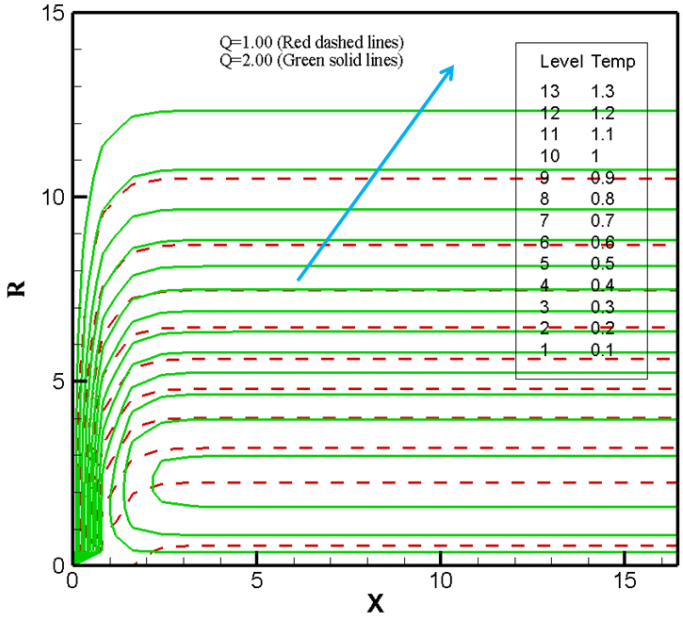

Figure 20 (a): Isotherms (contour view) for $Q = 1.00, 2.00$.

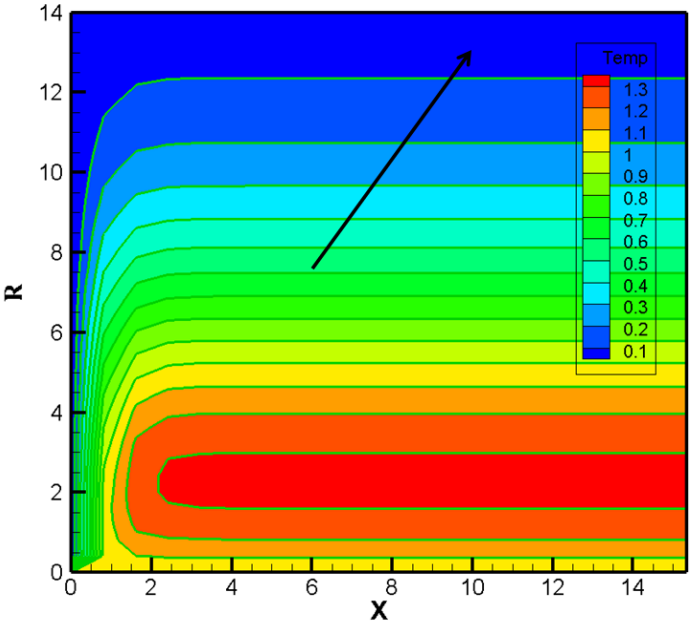

Figure 20 (b): Isotherms (flood and line view) for $Q = 1.00, 2.00$.

Once more, the contour flood view for a difference in the Grashof number and the Prandtl number is displayed in **Figures 18 (b)** to **19(b)**. **Figures 20 (a)** and **20(b)**, which show the effects of the heat source factor on isotherms in flood and line views, add to the isothermal lines. It should be noted that, under the conditions of the heat source values, the distribution of the thermal boundary layer thickness (the isotherm's line) increases with the expansion of Q from 1.0 to 2.0, as shown in **Figures-20(a)** and 2**0(b)**.

7. Conclusions

The unsteady MHD Casson fluid flow via a vertical cylindrical surface is numerically solved and the effects of thermal radiation and changing chemical reactions are investigated. Here is a summary of the main findings:

1. The velocity distribution decreases for the improving behaviour of the Magnetic parameter, and Casson term and increases for the Grashof number and heat source term.
2. Temperature outlines increase for increasing ethics heat source term whereas reduces for Prandtl number and thermal radiation.
3. The behaviour of concentration profiles decreases for the chemical reaction parameter and Lewis number and increases for the radiation parameter.
4. When the values of the Casson term get increased skin friction distributions are increasing and the opposite phenomenon is seen for rising data of magnetic parameter.
5. The Nusselt number profiles drop with the rise of the Grashof number and increase with the development of the Prandtl number.
6. The Sherwood number distribution increased owing to the increase of the Lewis number.
7. When Prandtl number data increase streamlines decrease, but streamlines and isothermal lines both increase as Grashof number and heat generation factor rise.

Acknowledgment. We thank the reviewers for their critical commonest for improving the presentation of the paper.

Author's Contributions. All the authors equally contributed in the paper.

Conflicts of interest. The authors declare that there are no conflicts of interest regarding the publication of this paper.

REFERENCES

1. S. Okay, Non-Newtonian blood flow in capillary with a permeable wall. In: Proc. Festschrift of Harold Wayland Symposium, *California Institute of Technology*, Pasadena, USA. (1979).
2. J. Boyd, J. M. Buick and S. Green, Analysis of Casson and Carreau–Yasuda non-Newtonian blood models in steady and oscillatory flow using the lattice Boltzmann method, *Physics of Fluids*, 19 (2007) 93-103.

3. M. A. Emmanuel, Y. S. Ibrahim and B. B. Letis, Analysis of Casson fluid flow over a vertical porous surface with chemical reaction in the presence of magnetic field, *Journal of Applied Mathematics*, 3 (2015) 713-723.
4. M. Y. Malik, M. Naseer, S. Nadeem and A. Rehman, The boundary layer flow of Casson nanofluid over a vertical exponentially stretching cylinder, *Applied Nanoscience*, 4 (2014) 869-873.
5. A. Hussanan, S. M. Zukhi, R. M. Tahar and I. Khan, Unsteady boundary layer flow and heat and mass transfer of a Casson fluid past an oscillating vertical plate with Newtonian heating, *PLoS ONE*, 9(2014) 08763.
6. T. Hayat, A. M. Bilal, S. A. Shehzad and A. Alsaedi, Mixed convection flow of Casson nanofluid over a stretching sheet with convectively heated chemical reaction and heat source/sink, *Journal of Applied Fluid Mechanics*, 8 (2015) 803-811.
7. G. Makanda, S. Shaw and P. Sibanda, Effects of radiation on MHD free convection of a Casson fluid from a horizontal circular cylinder with partial slip in non-Darcy porous medium with viscous dissipation, *Boundary Value Problems*, (2015) 75.
8. U. Mahabaleshwar and G. Lorenzini, Combined effect of heat source/sink and stress work on MHD Newtonian fluid flow over a stretching porous sheet, *International Journal of Heat and Technology*, 35(2017) 330-S335.
9. H. R. Kataria and H. R. Patel, Radiation and chemical reaction effects on MHD Casson fluid flow past an oscillating vertical plate embedded in porous medium, *Alexandria Engineering Journal*, 55(2016) 583-595.
10. M. S. Khan, I. Karim, L. E. Ali and A. Islam, Unsteady MHD free convection boundary layer flow of a nanofluid along a stretching sheet with thermal radiation and viscous dissipation effects, *International Nano Letters*, 2 (2012) 24.
11. S. Nadeem, R. U. Haq and C. Lee, MHD flow of Casson fluid over an exponentially shrinking sheet, *Scientia Iranica*, 19 (2012) 1550-1553.
12. P. K. Kumari, M. V. Murthy, M. Reddy and Y. V. K. Kumar, Peristaltic pumping of a magnetohydrodynamic Casson fluid in an inclined channel, *Advances in Applied Science Research*, 2 (2011) 428-436.
13. S. Sreenadh, A. R. Pallavi and B. Satynarayana, Flow of a Casson fluid through an inclined tube of mom-uniform cross section with multiple stenosis, *Advances in Applied Science Research*, 2 (2011) 340-349.
14. T. Sarker, S. M. Arifuzzaman, Sk. Reza-E-Rabbi, R. Ahmed, M.S. Khan and S.F. Ahmmed, Unsteady magnetohydrodynamic Casson nanofluid flow through a moving cylinder with Brownian and thermophoresis effects, *Annales de Chimie Science des Matériaux*, 2 (2018) 181-207.
15. T. Sarker, S. M. Arifuzzaman, Sk. Reza-E-Rabbi, M.S. Khan and S.F. Ahmmed, Computational Modelling of Chemically Reactive and Radiative Flow of Casson-Carreau Nanofluids Over an Inclined Cylindrical Surface with Bended Lorentz Force Presence in Porous Medium, *8th BSME International Conference on Thermal Engineering, AIP Conf. Proc.*, 2121(2019) 050006-1–050006-8.
16. T. Sarker, Sk. Reza-E-Rabbi, S. M. Arifuzzaman, R. Ahmed, M.S. Khan and S.F. Ahmmed, MHD Radiative Flow of Casson and Williamson Nanofluids over an Inclined Cylindrical Surface with Chemical Reaction Effects, *International Journal of Heat and Technology*, 37 (2019) 1117-1126.

17. C.A. Nandhini, S. Jothimani and A.J. Chamkha, Combined effect of radiation absorption and exponential parameter on chemically reactive Casson fluid over an exponentially stretching sheet, *Partial Differential Equations in Applied Mathematics*, 8 (2023) 100534.
18. K.K. Asogwa, B.S. Goud, Y.D. Reddy and A.A. Ibe, Suction effect on the dynamics of EMHD Casson nanofluid over an induced stagnation point flow of stretchable electromagnetic plate with radiation and chemical reaction, *Results in Engineering*, 15 (2022) 100518.
19. N.S. Yousef, A.M. Megahed, N.I. Ghoneim, M. Elsafi and E. Fares, Chemical reaction impact on MHD dissipative Casson-Williamson nanofluid flow over a slippery stretching sheet through porous medium, *Alexandria Engineering Journal*, 61(12) (2022) 10161–10170.
20. M.V. Krishna, Chemical reaction, heat absorption and Newtonian heating on MHD free convective Casson hybrid nanofluids past an infinite oscillating vertical porous plate, *International Communications in Heat and Mass Transfer*, 138 (2022) 106327.
21. R. Biswas, B.O. Falodun, N. Islam, S.F. Ahmmed, S.R. Mishra and M. Afikuzzaman, Computational modeling of Prandtl-nanofluid flow using exponentially vertical surface in terms of chemical reaction, *Engineering Reports*, e12747. (2023)
22. M.A. Sayeed, A. Podder, S.R. Mishra, M. Afikuzzaman and M.M. Alam, Computational modeling of unsteady MHD nanofluid over a cylinder using gyrotactic microorganisms, *Journal of Thermal Analysis and Calorimetry*,148(18) (2023), 1–16.
23. R. Biswas, M.S. Hossain, R. Islam, S.F. Ahmmed, S.R. Mishra and M. Afikuzzaman, Computational treatment of MHD Maxwell nanofluid flow across a stretching sheet considering higher-order chemical reaction and thermal radiation, *Journal of Computational Mathematics and Data Science*, 4 (2022) 100048.
24. D. Paul and G. Mandal, Magnetohydrodynamic nonlinear thermal radiative heat transfer of nanofluids over a flat plate in a porous medium in existence of variable thermal conductivity and chemical reaction, *International Journal of Ambient Energy*, 42(10) (2021) 1167–1177.
25. S. R. Raju, Unsteady MHD boundary layer flow of Casson fluid over an inclined surface embedded in a porous medium with thermal radiation and chemical reaction, *Journal of Nanofluids*, 7(4) (2018) 694–703.
26. P.S. Reddy and A.J. Chamkha, Soret and Dufour effects on MHD convective flow of Al_2O_3 – water and TiO_2- water nanofluids past a stretching sheet in porous media with heat generation/absorption, *Advanced Powder Technology*, 27 (2016) 1207–1218.
27. H.R. Kataria and H.R. Patel, Radiation and chemical reaction effects on MHD Casson fluid flow past an oscillating vertical plate embedded in porous medium, *Alexandria Engineering Journal*, 55 (2016) 583–595.
28. D.J. Samuel, Chemical reaction and melting heat effects on MHD free convective radiative fluid flow past a continuous moving plate in the presence of thermo-physical parameters, *Trans Tech Publications*, 384 (2018), 80–98.
29. B. Awasthi, Effects of heat and mass flux on MHD free convection flow through a porous medium in presence of radiation and chemical reaction, *Journal of Ultra Scientist of Physical Sciences*, 30(1) (2018) 20–31.

30. S. Shateyi and G.T. Marewo, Numerical solution of mixed convection flow of an MHD Jeffery fluid over an exponentially stretching sheet in the presence of thermal radiation and chemical reaction, *Open Physics,*16(1) (2018) 249–259.
31. A.A. Megahed, A.A. Hallool and H.A.E. Mky, Numerical solution of thermal radiation and joule-heating effects on an unsteady MHD with heat and mass transfer with chemical reaction, *International Journal of Advanced Research in Science, Engineering and Technology*, 5(2018) 2.
32. S. Reza-E-Rabbi, M. S. Khan, S. M. Arifuzzaman, S. Islam, P. Biswas, B. M. J. Rana, A. A. Mamun, T. Hayat and S. F. Ahmmed, Numerical simulation of a non-linear nanofluidic model to characterise the MHD chemically reactive flow past an inclined stretching surface, *Partial Differential Equations in Applied Mathematics,* 5 (2022).
33. Z. Benharkat, Rotating convective MHD flow over a vertical moving plate in the presence of heat source, radiation, chemical reaction and Hall effects, *Energy Thermofluids Eng.*, 2(1) (2022) 11–19.
34. M.R. Islam, R. Biswas, M. Hasan, M. Afikuzzaman and S.F. Ahmmed, Modeling of MHD Casson Fluid Flow Across an Infinite Vertical Plate with Effects of Brownian, Thermophoresis, and Chemical Reactivity, *Arabian Journal for Science and Engineering,* (2024) 2193-567X.
35. F. Ahmed, S. Reza-E-Rabbi, S.M. Ali, L.E. Ali, A. Islam, M. A. Rahman, R. Roy, M. R. Islam and S. F. Ahmmed, Numerical modeling of a MHD non-linear radiative Maxwell nanofluid with activation energy, *Heliyon,* 10 (2024) e24098.
36. A.K. Gautam, S. Rajput, K. Bhattacharyya, A.K. Pandey, A.J. Chamkha and M. Begum, Comparative study of two non-Newtonian fluids with bioconvective induced MHD flow in presence of multiple slips, heat source/sink and nonlinear thermal radiation, *Chemical Engineering Journal Advances,* 12 (2022) 100365.
37. M.Y. Ali, S. Reza-E-Rabbi, M.M.H. Rasel and S.F. Ahmmed, Combined impacts of thermoelectric and radiation on hydromagnetic nanofluid flow over a nonlinear stretching sheet, *Partial Differential Equations in Applied Mathematics,* 7 (2023) 100500.
38. S. Reza-E-Rabbi, S.F. Ahmmed, S. Islam, S.M. Arifuzzaman, B.M.J. Rana, M.Y. Ali and M.S. Khan, Characterization of fluid flow and heat transfer of a periodic magnetohydrodynamics nano non-Newtonian liquid with Arrhenius activation energy and nonlinear radiation, *Heat Transfer,* 51 (7) (2022) 6578–6615.
39. S. Li, K. Raghunath, A. Alfaleh, F. Ali, A. Zaib, M.I. Khan and V. Puneeth, Effects of activation energy and chemical reaction on unsteady MHD dissipative Darcy–Forchheimer squeezed flow of Casson fluid over horizontal channel, *Scientific Reports,* 13 (1) (2023) 2666.
40. P.S. Reddy, P. Sreedevi and A.J. Chamkha, Hybrid nanofluid heat and mass transfer characteristics over a stretching/shrinking sheet with slip effects, *Journal of Nanofluids,* 12 (1) (2023) 251–260.